Significant enhancement of magnetic anisotropy and conductivity in GaN/CrI_3 van der Waals heterostructures via electrostatic doping

Haoshen Ye,[1] Xiao Wang,[1] Dongmei Bai,[2] Junting Zhang,[1] Xiaoshan Wu,[3] G. P. Zhang,[4] and Jianli Wang[1,*]

[1]*School of Materials and Physics, China University of Mining and Technology, Xuzhou 221116, China*
[2]*School of Mathematics, China University of Mining and Technology, Xuzhou 221116, China*
[3]*National Lab of Solid State Microstructures, Nanjing University, Nanjing 210093, China*
[4]*Department of Physics, Indiana State University, Terre Haute, Indiana 47809, USA*

(Received 7 April 2021; revised 16 June 2021; accepted 5 August 2021; published 18 August 2021)

van der Waals magnetic heterostructures, consisting of a wide band-gap nitride semiconductor and an intrinsic ferromagnetic semiconductor, are potentially useful for low-dimensional spintronic field-effect transistors. However, there is a significant challenge. For instance, the integration often leads to a decreased Curie temperature, the magnetic anisotropy direction change, and low conductivities. Here, we employ the first-principles density-functional method to systematically investigate the electronic and magnetic properties of the GaN/CrI_3 van der Waals heterostructures under electrostatic doping. Though the easy magnetization axis of the monolayer CrI_3 transforms from out-of-plane to in-plane direction over 0.2 electron doping per unit cell, the GaN/CrI_3 van der Waals heterostructure maintains perpendicular anisotropy under electron doping, crucial for high-density information storage. The Curie temperature of the GaN/CrI_3 van der Waals heterostructure can be enhanced under both electron and hole doping. The GaN/CrI_3 van der Waals heterostructure presents half-metallic properties and the spin-up conductivities are much larger than that of the monolayer CrI_3 under the same electrostatic doping. Our results indicate that constructing heterostructures with ferromagnets and nonmagnetic semiconductors is an effective strategy for developing high-performance field-effect transistors.

DOI: 10.1103/PhysRevB.104.075433

I. INTRODUCTION

The integration of two-dimensional (2D) ferromagnets into field-effect transistors (FETs) promotes the development of spintronics and valleytronics [1,2], meeting the urgent demand for energy-efficient performance, miniaturization, and high density of the electronics. Constructing van der Waals (vdW) heterostructure has been proven to be an effective strategy to realize tunable magnetic devices [3,4]. Experimentally, entirely new magnetic and topological properties can be found in vdW heterostructures based on 2D ferromagnets and 2D nonmagnetic semiconductors due to the magnetic proximity-induced exchange interaction [5,6]. Meanwhile, ferromagnetic (FM) vdW heterostructures present flexible and interesting electronic and magnetic properties under conventional control methods, such as applying electric field [7], magnetic field [8], electrostatic doping [9], and so on. These results indicate promising applications of the combination of 2D ferromagnets and 2D nonmagnetic semiconductors in spintronics.

Graphenelike 2D gallium nitride (GaN) is a nonmagnetic semiconductor with an indirect band gap [10,11]. Theoretical calculations suggest that 2D GaN remains stable at high temperatures [12]. Experimentally, 2D GaN has been successfully realized via graphene encapsulation [13]. The 2D GaN and GaN-based vdW heterostructures are suitable for deep ultraviolet excitonic light sources and microcavity devices [14,15]. The carriers of 2D GaN are predicted to have high mobility, which shows potential for photocatalysis [16,17]. Besides, the high carrier mobility provides favorable conditions to enhance the transport properties of GaN-based vdW heterostructures. However, nonmagnetic 2D GaN has limited applications in spintronics. Two-dimensional chromium triiodide (CrI_3) is one of the ferromagnets most frequently used to fabricate magnetic devices [18,19]. Two-dimensional CrI_3 is a FM material with a Curie temperature (T_c) of 45 K [20]. Few-layer CrI_3 tunnel junction exhibits large magnetoresistance of 10 000% [21], presenting strong coupling between magnetism and electronic transport of vdW FM semiconductors. Though 2D CrI_3 has been integrated into different spin FETs experimentally, theoretical studies suggest that the electronic effective mass is large. The larger carrier effective mass tends to result in smaller carrier mobility, which is the main reason why the 2D CrI_3 seems more like an insulator rather than a semiconductor [22]. Both effective mass and mobility play decisive roles in the electrical transport performance of FETs. The electrical transport performance of materials can be improved by constructing vdW heterostructure [23].

Here, we construct vdW heterostructures based on 2D GaN and 2D CrI_3. The electronic, magnetic, and transport properties of GaN/CrI_3 vdW heterostructures are systematically investigated via first-principles calculations. Meanwhile, the effects of electrostatic doping are also considered for stable vdW heterostructures. Our calculations show that the GaN/CrI_3 vdW heterostructures present higher T_c, the

*jlwang@cumt.edu.cn

robustness of the easy magnetization axis (EMA), and superior spin-dependent conductivities compared to the isolated GaN and CrI_3. This paper is organized as follows. In Sec. II, we present the computational methods and details. In Sec. III A, we determine the structure and magnetic ground of GaN/CrI_3 vdW heterostructures. The magnetic anisotropy is investigated and T_c is calculated in Sec. III B. Finally, the spin-dependent transport properties are presented in Sec. III C. In Sec. IV, we briefly conclude our results and findings.

II. METHODOLOGY

We employ the first-principles calculations density-functional method as implemented in the Vienna *Ab-initio* Simulation Package (VASP) with projector augmented-wave method [24]. The exchange-correlation potential is approximated in the form of Perdew-Burke-Ernzerhof functional [25]. Generalized gradient approximation plus U(GGA+U) is adopted to describe the 3*d* orbitals of the Cr atoms [26], in which the Hubbard U parameter of 2.63 eV is calculated based on random-phase approximation [27,28]. In the calculations of Hubbard U parameters, the t_{2g} orbitals of Cr atoms are selected as the orbital projections by the means of maximally localized Wannier functions, which are implemented in the WANNIER90 code [29,30]. The D3 Grimme correction was adopted for the consideration of vdW interaction in all computational processes [31]. A 20-Å vacuum is applied along the out-of-plane direction to avoid the interaction between the neighboring unit cell. Plane-wave cutoff energy of 500 eV is used for all calculations. Numerical integration over the Brillouin zone is performed with a Γ-centered $8\times8\times1$ k-point mesh. Both the lattice constants and the atomic positions are relaxed fully until energy and force converge to 10^{-5} eV and 0.01 V/Å, respectively. The band structures are obtained by using Heyd-Scuseria-Ernzerhof hybrid functional (HSE06) [32], which can provide more accurate values of band gaps [33]. Spin-orbit coupling (SOC) is switched on in the calculation of magnetic anisotropy energy (MAE) [34]. All ionic positions are fully relaxed with fixed lattice constants under electrostatic doping. For the GaN/CrI_3 vdW heterostructure, $2\times2\times1$ supercells are constructed for phonon spectra calculations. The spin-polarized electronic transport properties are calculated with the semiclassical Boltzmann transport theory, using BOLTZTRAP2 code [35]. The transport properties are calculated in a temperature range of 30–90 K. The temperature and energy-dependent relaxation time is obtained by the deformation potential theory [36].

III. RESULTS AND DISCUSSION

A. Stabilities and electronic properties

Four magnetic configurations (see Fig. S1 in Supplemental Material [37]) for monolayer CrI_3 and three typical stacking configurations [Fig. 1(a)] are considered for GaN/CrI_3 vdW heterostructure, respectively. It should be mentioned that 2D GaN can be planar and buckled. However, under the limitation of monolayer structure, the planar structure has been proven the energetically most favorable structure for monolayer GaN [38]. Though hydrogen passivation can preserve the buckled structure of monolayer GaN, obvious

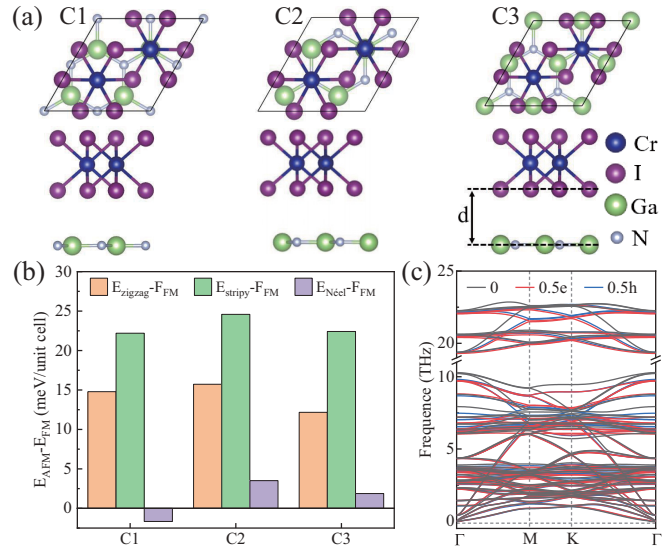

FIG. 1. (a) Three typical stacking configurations, (b) the energy difference between AFM and FM configuration of GaN/CrI_3 vdW heterostructures at GGA+U level, and (c) phonon spectra of stacking C3 with and without carrier doping.

imaginary modes exist in the phonon spectrum (see Fig. S3(c) in Supplemental Material [37]). Therefore, planar GaN is chosen in our work. The lattice constants of monolayer GaN and monolayer CrI_3 are 3.20 Å [11] and 6.97 Å, which are consistent well with the previous works [39,40]. The unit cell of the GaN/CrI_3 vdW heterostructure is composed of a $2\times2\times1$ supercell of the monolayer GaN. The lattice constants of the GaN/CrI_3 vdW heterostructures are similar for different stacking configurations. Both the C2 and the C3 stacking configurations favor FM ground state with the magnetic moment of 6.0 μ_B/unit-cell. The C1 stacking configuration favors Néel AFM ground state with the magnetic moment of 0 μ_B/unit-cell (see Table SI in Supplemental Material [37]). The binding energies (E_b) are calculated as

$$E_b = E_{\mathrm{GaN/CrI_3}} - E_{\mathrm{GaN}} - E_{\mathrm{CrI_3}},$$

where $E_{\mathrm{GaN/CrI_3}}$, E_{GaN}, and $E_{\mathrm{CrI_3}}$ are the total energy of the GaN/CrI_3 vdW heterostructures, monolayer GaN, and monolayer CrI_3, respectively. We focus on the C3 stacking configuration whose E_b is the lowest among the three stacking configurations. Imaginary modes exist in the phonon spectra of C1 and C2 stackings (see Figs. S5(a) and S5(b) in Supplemental Material [37]), and no imaginary modes exist in phonon spectrum [Fig. 1(c)], which indicates good dynamical stability of the GaN/CrI_3 vdW heterostructures with C3 stacking configuration.

The band structures of the monolayer GaN and monolayer CrI_3 are presented in Fig. S3 (see Supplemental Material [37]). The band gap of the monolayer GaN is 3.23 eV. The band gaps of the monolayer CrI_3 are 1.77 and 3.78 eV for the spin-up and spin-down channels, respectively. The projected band structures of the GaN/CrI_3 vdW heterostructure are presented in Fig. 2. Due to the octahedral crystal field, the 3*d* orbitals of the Cr atoms are split into two groups: the double e_g and the triple t_{2g} orbitals. For the spin-up channels,

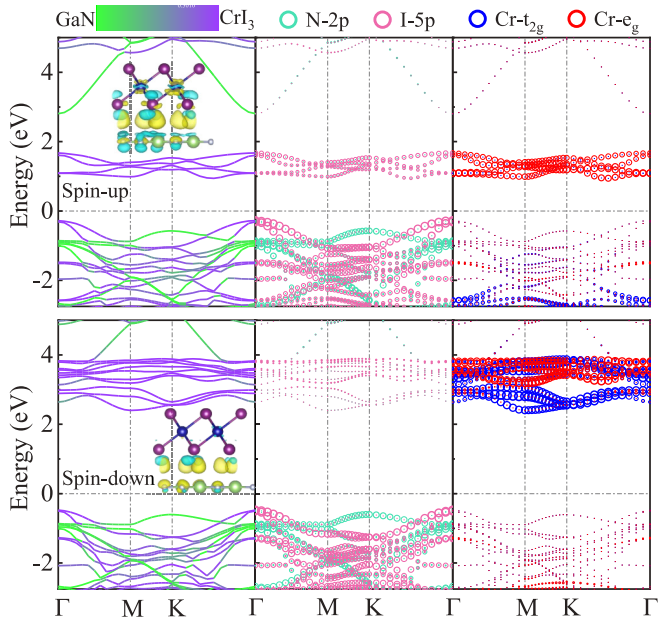

FIG. 2. The projected band structure of the GaN/CrI_3 vdW heterostructure at HSE06 level. The yellow and blue distribution of the insets correspond to charge accumulation and depletion with the isosurface of 0.0002 e Å^{-3}.

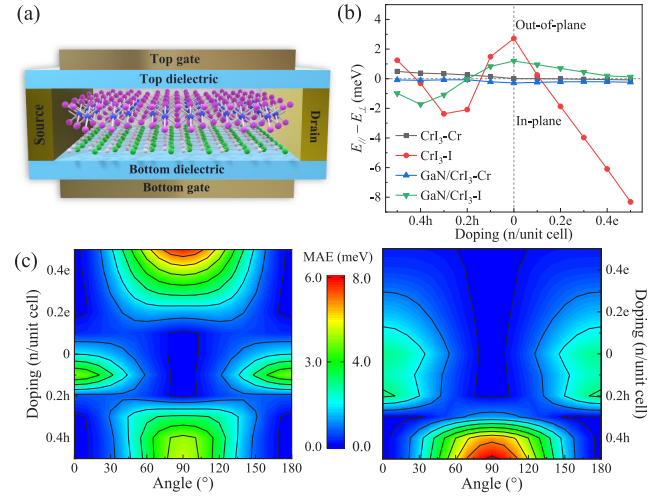

FIG. 3. (a) Schematic of a dual-gate FET based on the GaN/CrI_3 vdW heterostructure. (b) The calculated $E_\parallel - E_\perp$ of Cr and iodine atoms in the monolayer CrI_3 and GaN/CrI_3 vdW heterostructure at GGA+U+SOC level, respectively. (c) The total MAE of monolayer CrI_3 (left) and GaN/CrI_3 vdW heterostructure (right), respectively. The left and right scales of the color bar are for the monolayer CrI_3 and GaN/CrI_3 vdW heterostructure, respectively.

the valence-band maximum (VBM) is mainly contributed by the 5p orbitals of the iodine atoms, and the conduction-band minimum (CBM) is contributed by the 5p orbitals of the iodine atoms and the e_g orbitals of the Cr atoms. As for the spin-down channels, both the VBM and CBM are contributed by the 5p orbitals of the iodine atoms and the t_{2g} orbitals of the Cr atoms, respectively. The band gaps are 1.22 and 2.88 eV for the spin-up and spin-down channels, respectively. Therefore, both the spin-up and spin-down channels present type-I band alignment. As presented in the insets of Fig. 2, complex charge rearrangement happens after constructing the GaN/CrI_3 vdW heterostructure, which reveals strong interlayer interaction between the GaN layer and the CrI_3 layer.

B. Magnetic anisotropy and Curie temperatures

Electrostatic doping is a novel way to modify carrier concentration in a dual-gate FET [9,41]. Figure 3(a) presents a schematic of a dual-gate FET based on GaN/CrI_3 vdW heterostructure, where the GaN/CrI_3 vdW heterostructure is encapsulated by two dielectric layer and two gates. We consider a doping concentration within 1.36×10^{14} cm^{-2}, corresponding to 0.5 hole (h) or 0.5 electron (e) doping per unit cell. Experimentally, the doping concentration of $10^{13} \sim 10^{15}$ cm^{-2} can be realized [42–44]. The magnetic ground states of monolayer CrI_3 and GaN/CrI_3 vdW heterostructure are FM under electrostatic doping (see Fig. S4 in Supplemental Material [37]). No spurious charge exists in the vacuum region under electrostatic doping, which is proved via Bader charge analysis and charge difference (see Figs. S4 and S5 in Supplemental Material [37]). Due to the important role of MAE and T_c in practical applications, we carried out calculations on the MAE under different doping concentrations. As presented in Fig. 3(c), the MAE is calculated by setting magnetic axes along different directions and the angles with the lowest MAE are the EMAs. The results indicate that the EMA of CrI_3 changes from out-of-plane direction to in-plane direction when doping concentration is over 0.3 h/unit-cell or 0.2 e/unit-cell. Note that perpendicular magnetization anisotropy is crucial for high-density information storage [45]. As for the GaN/CrI_3 vdW heterostructure, the EMA can remain out-of-plane direction 0.3 $h \sim 0.5$ e/unit-cell doping. As shown in Fig. 3(b), the MAE of both the monolayer CrI_3 and GaN/CrI_3 vdW heterostructure are largely contributed by the iodine atoms, while Cr atoms present negligible contribution to MAE under electrostatic doping. Our results of the monolayer CrI_3 are consistent with the previous works [11,46]. The doping-induced transformation of magnetic anisotropy can be explained from the second-order perturbation theory analysis [47]. The SOC-induced MAE is given by

$$E^{\mathrm{SL}} = \sum_o \sum_u \frac{|\langle o|H^{\mathrm{SL}}|u\rangle|^2}{E_u - E_o},$$

where o and u correspond to the occupied and unoccupied states near the Fermi energy level, respectively; E_o and E_u are the energy levels of the states. $H^{\mathrm{SL}} = \xi \vec{\sigma} \cdot \vec{L}$, where ξ, $\vec{\sigma}$, and $\vec{L}$ are the SOC constant, Pauli matrix, and orbital angular momentum operator, respectively. When the directions perpendicular ($\perp$) and parallel ($\parallel$) to the plane are defined as the out-of-plane and in-plane direction, respectively, the MAE can be calculated via

$$\Delta E = E_\parallel - E_\perp = \pm\xi^2 \sum_{o,u} \frac{|\langle o|L_z|u\rangle|^2 - |\langle o|L_x|u\rangle|^2}{E_u - E_o},$$

where $\pm$ is decided by the spin states of the occupied and unoccupied states ($+$ and $-$ for parallel and opposite spin states,

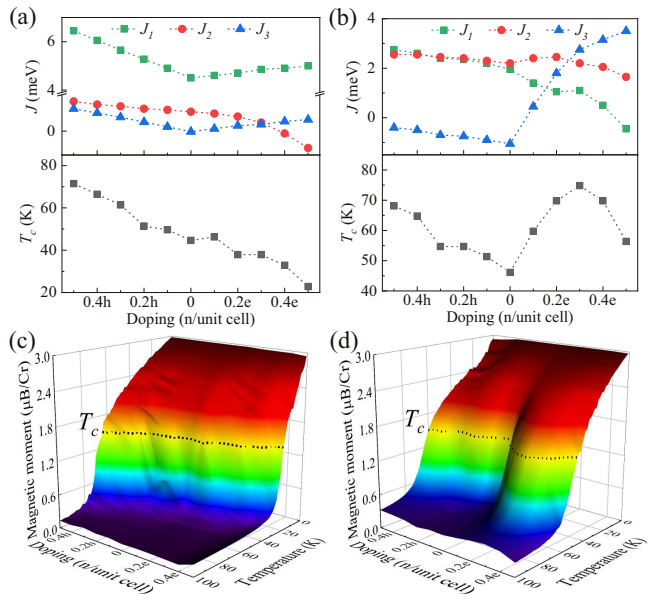

FIG. 4. The exchange parameters at GGA+U level and T_c of (a) monolayer CrI_3 and (b) GaN/CrI_3 vdW heterostructure under electrostatic doping. The simulated average magnetic moment of Cr atoms of (c) monolayer CrI_3 and (d) GaN/CrI_3 vdW heterostructure under electrostatic doping.

respectively). More details are presented in Part III of Supplemental Material [37]. As shown in Fig. 2, the highest occupied states are the $5p$ orbitals of the iodine atoms, while the occupied t_{2g} states of the Cr atoms are much lower. Therefore, the Cr atoms contribute little to the MAE. In the cases of electrostatic doping, the $5p$ orbitals of iodine atoms are the main acceptor of the extra holes and electrons, which means the occupancy of the iodine atoms varies under electrostatic doping. However, the occupied t_{2g} states of the Cr atoms cannot be changed. Therefore, the MAE of the iodine atoms is sensitive to electrostatic doping and the iodine atoms dominate the transformation of EMA. The CrI_3 layer in GaN/CrI_3 vdW heterostructure obtains fewer extra carriers than the isolated CrI_3 under the same concentration of electrostatic doping. Meanwhile, the GaN layer makes no contributions to MAE. Consequently, the MAE of the GaN/CrI_3 vdW heterostructure changes more gently than that of the monolayer CrI_3.

Based on the Heisenberg model, the T_c of the systems is estimated by Monte Carlo simulation. We consider the first-, second-, and third-nearest exchange interactions and magnetic anisotropy. The spin Hamiltonian can be written as [48]

$$H = -J_{ij}\sum_{ij}\vec{S}_i\cdot\vec{S}_j - A_i\sum_i(\vec{S}_i\cdot\vec{z}_i)^2,$$

where, J_{ij} is exchange parameters between site i and j, containing the first- (J_1), second- (J_2), and third-nearest (J_3) exchange interactions (see Fig. S2(a) in Supplemental Material [37]). A_i is single-ion anisotropy constant [49], and $\vec{z}_i$ is the unit vector long EMA, respectively. The calculated exchange interaction parameters under electrostatic doping are presented in Figs. 4(a) and 4(b) for the monolayer CrI_3 and GaN/CrI_3 vdW heterostructure, respectively. The simulated average magnetic moments of Cr atoms under electrostatic doping are presented in Figs. 4(c) and 4(d), respectively. The simulated T_c without doping is 45 and 46 K for monolayer CrI_3 and GaN/CrI_3 vdW heterostructure, respectively. The simulated T_c of the monolayer CrI_3 is in great agreement with the experimental value [20]. The T_c of monolayer CrI_3 can be enhanced via hole doping. However, under electron doping, the T_c of monolayer CrI_3 is decreased. That is, hole doping helps stabilize FM order of monolayer CrI_3. The same evolution of magnetism under electrostatic doping is also found in 2D VSe_2 [50]. The highest T_c of 71 K is realized under 0.5 h/unit-cell doping, which decreases as electrons doping and the lowest T_c is 23 K at 0.5 e/unit-cell doping. As for the GaN/CrI_3 vdW heterostructure, both holes and electrons doping can enhance the T_c. The highest T_c of 75 K can be realized at 0.3 e/unit-cell doping. Ferromagnetism of CrI_3 can be enhanced by constructing vdW heterostructure [51], which may attribute to additional possible superexchange interactions in the form of Cr-N-Cr induced by GaN (see Fig. S2(b) in Supplemental Material [37]).

C. Temperatures, electrostatic doping, and spin-dependent transport properties

Electronic transport properties are also crucial for the practical applications of spintronic devices. The spin-dependent transport properties are calculated within the semiclassical Boltzmann transport theory. The conductivity along the α direction is calculated via [52]

$$\sigma_{\alpha\alpha} = \frac{e^2}{V}\int \tau\cdot v_\alpha^2\left[-\frac{\partial f_0(T,E)}{\partial E}\right]dE,$$

where V is the volume of the unit cells, v_α is the group velocity, $f_0(T,E) = (e^{(E-E_f)/k_BT}+1)^{-1}$ is the Fermi-Dirac distribution function, k_B is the Boltzmann constant, E_f is the Fermi energy level, and T is temperature. The energy-dependent relaxation time τ of carriers is given by $\tau(T,E) = \tau_0(T)(E - E_{\mathrm{VBM/CBM}})/k_BT$ [53], where E_{VBM} and E_{CBM} are the energy of VBM and CBM in the cases of hole doping and electron doping, respectively. The reference relaxation time τ_0 is obtained from the deformation potential theory [36]:

$$\tau_0 = \frac{\hbar^3 C_{2D}}{k_BT m_d (E_l)^2},$$

where $\hbar$, C_{2D}, $m_d = \sqrt{m_x^* m_y^*}$, and E_l are the reduced Planck constant, elastic modulus, average effective mass, and deformation potential constant, respectively, which are shown in Table I. The x and y directions correspond to the zigzag and armchair directions, respectively. These results are consistent with the previous works [54–56] and more details of the calculations are presented in Part IV of Supplemental Material [37]. Besides, we can obtain the mobility of carriers via $\mu = \tau e/m^*$, where τ and m^* are relaxation time and effective mass of carriers, respectively. The calculated mobilities are presented in Fig. 5. The mobility of holes is much larger than that of the electrons in monolayer GaN. The mobilities of spin-down carriers in monolayer CrI_3 are much larger than that of the spin-up carriers, which is due to the low effective

TABLE I. Calculated elastic modulus C_{2D} (N/m), effective mass m^* (m_e), and deformation potential constant E_l (eV) of different systems. Results of spin-up and spin-down states are separated by the slashes.

System	C_{2D}	Direction	m_e^*	m_h^*	E_l^e	E_l^h
GaN	140.12	Zigzag	0.26/0.26	1.33/1.33	−10.42/−10.42	−0.85/−0.85
		Armchair	0.28/0.28	1.27/1.27	−10.40/−10.40	−0.91/−0.91
CrI_3	27.79	Zigzag	2.38/2.04	1.37/1.10	−4.95/−2.19	−6.97/−7.48
		Armchair	40.26/0.70	3.32/1.46	−4.94/−1.41	−7.19/−7.62
GaN/CrI_3	165.84	Zigzag	0.58/0.32	1.31/0.82	−4.24/−3.43	−10.71/−10.53
		Armchair	2.11/0.29	1.28/0.96	−4.94/−2.72	−10.07/−11.72

mass of spin-down carriers. The mobilities are enhanced in GaN/CrI_3 vdW heterostructure. Similar to the monolayer CrI_3, the mobilities of spin-down carriers are larger than that of the spin-up carriers in GaN/CrI_3 vdW heterostructure.

Figure 6 presents the calculated spin-up conductivities of monolayer GaN, monolayer CrI_3, and GaN/CrI_3 vdW heterostructure, respectively. The monolayer GaN presents high conductivities along both the zigzag and armchair directions. The conductivities of the monolayer CrI_3 are almost $10^2 \sim 10^3$ times lower than that of the monolayer GaN under the same temperature and electrostatic doping. Meanwhile, the conductivity of the monolayer CrI_3 along the armchair direction is much lower than that of the zigzag direction under electrons doping, which may attribute to the much larger effective mass of electrons along the armchair direction. As presented in Figs. 6(c) and 6(d), the conductivities are enhanced appreciably after constructing the GaN/CrI_3 vdW heterostructure, especially the armchair direction. The conductivity along the armchair direction is enhanced by over 10^2 times. The spin-down conductivities are presented in Fig. S14 of Supplemental Material [37]. Though the spin-down carriers in monolayer CrI_3 and GaN/CrI_3 vdW heterostructure present higher mobilities, the spin-down channel is insulated from the large band gap. The spin-down channels of CrI_3 are completely insulated under 0.5 $h \sim 0.5$ e/unit-cell doping, and the spin-down channels of GaN/CrI_3 vdW heterostructure are also insulated under 0.3 $h \sim 0.5$ e/unit-cell doping (see Fig. S14 in Supplemental Material [37]). For the monolayer CrI_3 and GaN/CrI_3 vdW heterostructure, the spin-down channels are almost insulated due to the absence of spin-down states at the Fermi energy level, which means pure spin-up polarized current can be realized. As discussed above, the direction of the EMA of monolayer CrI_3 changes over 0.2 e/unit-cell doping, limiting its application in high-density information storage. Therefore, the GaN/CrI_3 vdW heterostructure is a promising candidate for low-dimensional spintronic FETs with higher conductivity, higher T_c, and stability of EMA.

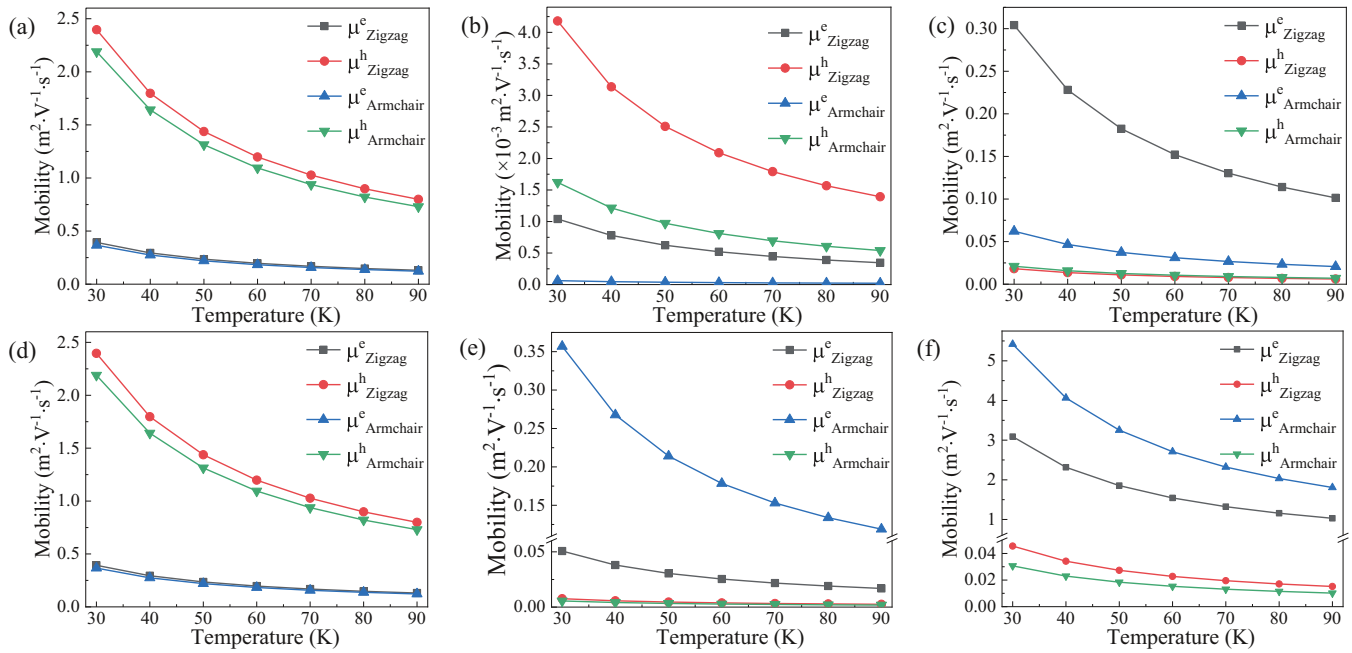

FIG. 5. Calculated mobilities of spin-up carriers for (a) monolayer GaN, (b) monolayer CrI_3, and (c) GaN/CrI_3 vdW heterostructure, respectively. Calculated mobilities of spin-down carriers for (d) monolayer GaN, (e) monolayer CrI_3, and (f) GaN/CrI_3 vdW heterostructure, respectively.

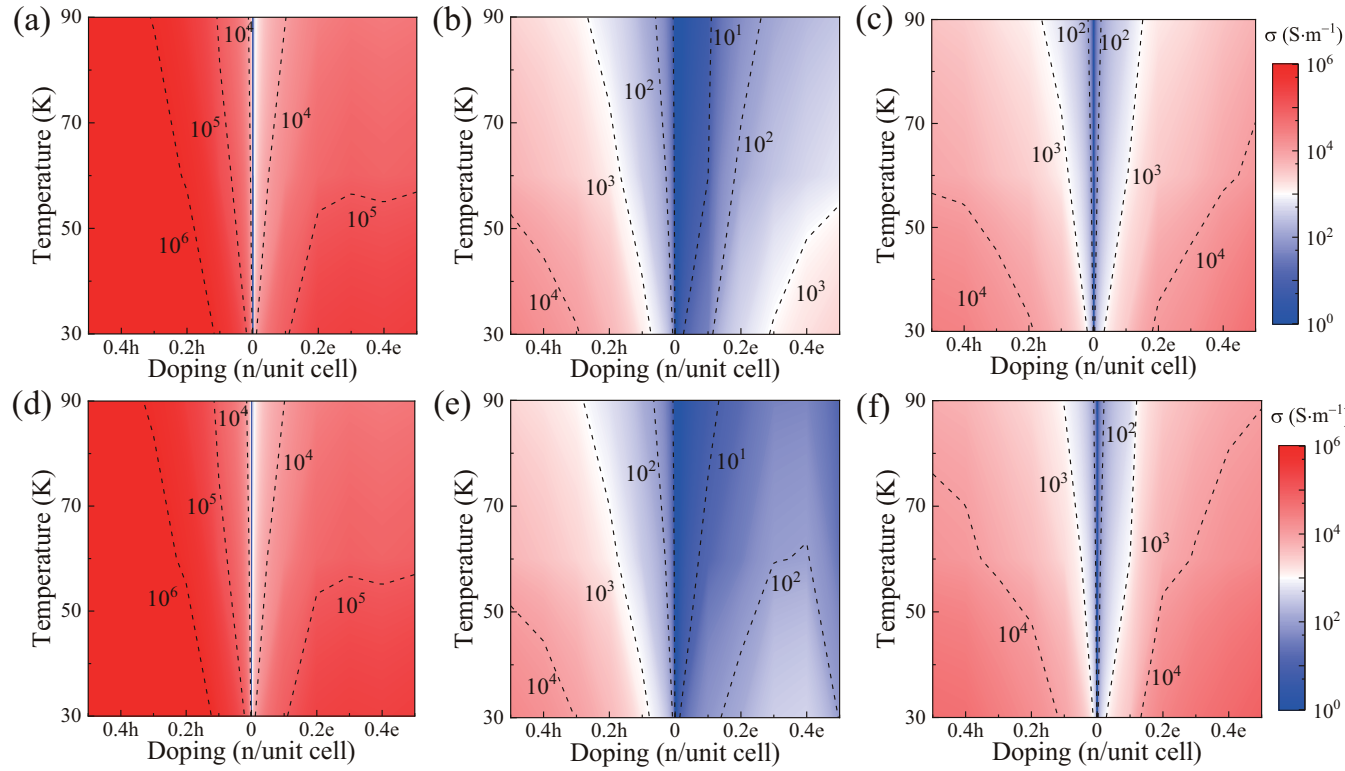

FIG. 6. Temperature and electrostatic doping-dependent resolved spin-up conductivities of (a) monolayer GaN, (b) monolayer CrI_3, and (c) GaN/CrI_3 vdW heterostructure along the zigzag direction, respectively. (d)–(f) The corresponding spin-up conductivities along the armchair direction.

IV. CONCLUSIONS

We have proposed that the combination of nonmagnetic semiconductor GaN and ferromagnet CrI_3 can provide enhanced MAE, T_c, and spin-resolved conductivities for dual-gate FETs. The decreased T_c, the change of EMA, and the low conductivities of the monolayer CrI_3 under electrons doping will limit its potential applications in future nanoscale spintronic devices. Interestingly, these issues are partially resolved in the GaN/CrI_3 vdW heterostructure. The T_c of the GaN/CrI_3 vdW heterostructure can be enhanced under both electron and hole doping. The direction of EMA remains along the out-of-plane direction under electron doping, which is highly desired in high-density information storage. Meanwhile, pure spin-up polarized current and appreciable enhancement of the spin-up conductivity can be realized through constructing heterostructure with 2D GaN. Our findings suggest that the vdW heterostructure engineering may be an effective method to realize enhanced T_c, robust EMA, and high conductivities for low-dimensional spintronics.

ACKNOWLEDGMENTS

This work has been supported by the Fundamental Research Funds for the Central Universities under Grant No. 2020ZDPYMS28, the Postgraduate Research & Practice Innovation Program of Jiangsu Province (Grant No. KYCX21_2155), and the Assistance Program for Future Outstanding Talents of China University of Mining and Technology (Grant No. 2021WLJCRCZL168). We are grateful to the High-Performance Computing Center of China University of Mining and Technology for the award of CPU hours to accomplish this work.

[1] V. P. Ningrum, B. W. Liu, W. Wang, Y. Yin, Y. Cao, C. Y. Zha, H. G. Xie, X. H. Jiang, Y. Sun, S. C. Qin, X. L. Chen, T. S. Qin, C. Zhu, L. Wang, and W. Huang, Recent advances in two-dimensional magnets: Physics and devices towards spintronic applications, Research **2020**, 1768918 (2020).

[2] S. W. Jiang, L. Z. Li, Z. F. Wang, J. Shan, and K. F. Mak, Spin tunnel field-effect transistors based on two-dimensional van der Waals heterostructures, Nat. Electron. **2**, 159 (2019).

[3] S. Husain, R. Gupta, A. Kumar, P. Kumar, N. Behera, R. Brucas, S. Chaudhary, and P. Svedlindh, Emergence of spin–orbit torques in 2D transition metal dichalcogenides: A status update, Appl. Phys. Rev. **7**, 041312 (2020).

[4] F. Herling, C. K. Safeer, J. Ingla-Aynés, N. Ontoso, L. E. Hueso, and F. Casanova, Gate tunability of highly efficient spin-to-charge conversion by spin Hall effect in graphene proximitized with WSe_2, APL Mater. **8**, 071103 (2020).

[5] D. Zhong, K. L. Seyler, X. Y. Linpeng, N. P. Wilson, T. Taniguchi, K. Watanabe, M. A. McGuire, K. M. C. Fu, D. Xiao, W. Yao, and X. D. Xu, Layer-resolved magnetic proximity effect in van der Waals heterostructures, Nat. Nanotechnol. **15**, 187 (2020).

[6] Y. Wu, S. F. Zhang, J. W. Zhang, W. Wang, Y. L. Zhu, J. Hu, G. Yin, K. Wong, C. Fang, C. H. Wan, X. F. Han, Q. M. Shao, T. Taniguchi, K. Watanabe, J. D. Zang, Z. Q. Mao, X. X. Zhang, and K. L. Wang, Néel-type skyrmion in WTe_2/Fe_3GeTe_2 van der Waals heterostructure, Nat. Commun. **11**, 3860 (2020).

[7] L. Ciorciaro, M. Kroner, K. Watanabe, T. Taniguchi, and A. Imamoglu, Observation of Magnetic Proximity Effect Using Resonant Optical Spectroscopy of an Electrically Tunable $MoSe_2/CrBr_3$ Heterostructure, Phys. Rev. Lett. **124**, 197401 (2020).

[8] H. L. Lin, F. G. Yan, C. Hu, Q. S. Lv, W. K. Zhu, Z. Wang, Z. M. Wei, K. Chang, and K. Y. Wang, Spin-valve effect in $Fe_3GeTe_2/MoS_2/Fe_3GeTe_2$ van der Waals heterostructures, ACS Appl. Mater. Interfaces **12**, 43921 (2020).

[9] S. W. Jiang, L. Z. Li, Z. F. Wang, K. F. Mak, and J. Shan, Controlling magnetism in 2D CrI_3 by electrostatic doping, Nat. Nanotechnol. **13**, 549 (2018).

[10] H. B. Shu, X. Niu, X. J. Ding, and Y. Wang, Effects of strain and surface modification on stability, electronic and optical properties of GaN monolayer, Appl. Surf. Sci. **479**, 475 (2019).

[11] H. S. Ye, Y. J. Zhu, D. M. Bai, J. T. Zhang, X. S. Wu, and J. L. Wang, Spin valve effect in VN/GaN/VN van der Waals heterostructures, Phys. Rev. B **103**, 035423 (2021).

[12] A. Onen, D. Kecik, E. Durgun, and S. Ciraci, GaN: From three- to two-dimensional single-layer crystal and its multilayer van der Waals solids, Phys. Rev. B **93**, 085431 (2016).

[13] Z. Y. Al Balushi, K. Wang, R. K. Ghosh, R. A. Vila, S. M. Eichfeld, J. D. Caldwell, X. Qin, Y. C. Lin, P. A. DeSario, G. Stone, S. Subramanian, D. F. Paul, R. M. Wallace, S. Datta, J. M. Redwing, and J. A. Robinson, Two-dimensional gallium nitride realized via graphene encapsulation, Nat. Mater. **15**, 1166 (2016).

[14] A. Aiello, Y. Wu, A. Pandey, P. Wang, W. Lee, D. Bayerl, N. Sanders, Z. Deng, J. Gim, K. Sun, R. Hovden, E. Kioupakis, Z. Mi, and P. Bhattacharya, Deep ultraviolet luminescence due to extreme confinement in monolayer GaN/Al(Ga)N nanowire and planar heterostructures, Nano Lett. **19**, 7852 (2019).

[15] Y. Wu, X. Liu, P. Wang, D. A. Laleyan, K. Sun, Y. Sun, C. Ahn, M. Kira, E. Kioupakis, and Z. Mi, Monolayer GaN excitonic deep ultraviolet light emitting diodes, Appl. Phys. Lett. **116**, 013101 (2020).

[16] M. A. Hassan, M. W. Kim, M. A. Johar, A. Waseem, M. K. Kwon, and S. W. Ryu, Transferred monolayer MoS_2 onto GaN for heterostructure photoanode: Toward stable and efficient photoelectrochemical water splitting, Sci. Rep. **9**, 20141 (2019).

[17] J. Li, W. J. Yang, A. M. Wu, X. L. Zhang, T. T. Xu, and B. D. Liu, Band-gap tunable 2D hexagonal $(GaN)_{1-x}(ZnO)_x$ solid-solution nanosheets for photocatalytic water splitting, ACS Appl. Mater. Interfaces **12**, 8583 (2020).

[18] T. C. Song, Z. Y. Fei, M. Yankowitz, Z. Lin, Q. N. Jiang, K. Hwangbo, Q. Zhang, B. S. Sun, T. Taniguchi, K. Watanabe, M. A. McGuire, D. Graf, T. Cao, J. H. Chu, D. H. Cobden, C. R. Dean, D. Xiao, and X. D. Xu, Switching 2D magnetic states via pressure tuning of layer stacking, Nat. Mater. **18**, 1298 (2019).

[19] W. J. Zhao, Z. Y. Fei, T. C. Song, H. K. Choi, T. Palomaki, B. S. Sun, P. Malinowski, M. A. McGuire, J. H. Chu, X. D. Xu, and D. H. Cobden, Magnetic proximity and nonreciprocal current switching in a monolayer WTe_2 helical edge, Nat. Mater. **19**, 503 (2020).

[20] B. Huang, G. Clark, E. Navarro-Moratalla, D. R. Klein, R. Cheng, K. L. Seyler, D. Zhong, E. Schmidgall, M. A. McGuire, D. H. Cobden, W. Yao, D. Xiao, P. Jarillo-Herrero, and X. Xu, Layer-dependent ferromagnetism in a van der Waals crystal down to the monolayer limit, Nature (London) **546**, 270 (2017).

[21] Z. Wang, I. Gutierrez-Lezama, N. Ubrig, M. Kroner, M. Gibertini, T. Taniguchi, K. Watanabe, A. Imamoglu, E. Giannini, and A. F. Morpurgo, Very large tunneling magnetoresistance in layered magnetic semiconductor CrI_3, Nat. Commun. **9**, 2516 (2018).

[22] C. Q. Lin, Y. R. Li, Q. L. Wei, Q. Shen, Y. C. Cheng, and W. Huang, Enhanced valley splitting of transition-metal dichalcogenide by vacancies in robust ferromagnetic insulating chromium trihalides, ACS Appl. Mater. Interfaces **11**, 18858 (2019).

[23] L. Xu, Y. Y. Wang, C. H. Hsiao, I. C. Ni, M. H. Chen, and C. I. Wu, Enhanced electrical performance of van der Waals heterostructure, Adv. Mater. Interfaces **8**, 2001850 (2021).

[24] G. Kresse and J. Furthmüller, Efficient iterative schemes for ab initio total-energy calculations using a plane-wave basis set, Phys. Rev. B **54**, 11169 (1996).

[25] J. P. Perdew, K. Burke, and M. Ernzerhof, Generalized Gradient Approximation Made Simple, Phys. Rev. Lett. **77**, 3865 (1996).

[26] S. L. Dudarev, G. A. Botton, S. Y. Savrasov, C. J. Humphreys, and A. P. Sutton, Electron-energy-loss spectra and the structural stability of nickel oxide: An LSDA+U study, Phys. Rev. B **57**, 1505 (1998).

[27] F. Aryasetiawan, K. Karlsson, O. Jepsen, and U. Schönberger, Calculations of Hubbard U from first-principles, Phys. Rev. B **74**, 125106 (2006).

[28] L. Vaugier, H. Jiang, and S. Biermann, Hubbard U and Hund exchange J in transition metal oxides: Screening versus localization trends from constrained random phase approximation, Phys. Rev. B **86**, 165105 (2012).

[29] A. A. Mostofi, J. R. Yates, Y.-S. Lee, I. Souza, D. Vanderbilt, and N. Marzari, wannier90: A tool for obtaining maximally-localised Wannier functions, Comput. Phys. Commun. **178**, 685 (2008).

[30] A. A. Mostofi, J. R. Yates, G. Pizzi, Y.-S. Lee, I. Souza, D. Vanderbilt, and N. Marzari, An updated version of wannier90: A tool for obtaining maximally-localised Wannier functions, Comput. Phys. Commun. **185**, 2309 (2014).

[31] S. Grimme, J. Antony, S. Ehrlich, and H. Krieg, A consistent and accurate ab initio parametrization of density functional dispersion correction (DFT-D) for the 94 elements H-Pu, J. Chem. Phys. **132**, 154104 (2010).

[32] J. Heyd, G. E. Scuseria, and M. Ernzerhof, Hybrid functionals based on a screened Coulomb potential, J. Chem. Phys. **118**, 8207 (2003).

[33] Á. Morales-García, R. Valero, and F. Illas, An empirical, yet practical way to predict the band gap in solids by using density functional band structure calculations, J. Phys. Chem. C **121**, 18862 (2017).

[34] G. H. O. Daalderop, P. J. Kelly, and M. F. H. Schuurmans, First-principles calculation of the magnetocrystalline anisotropy

energy of iron, cobalt, and nickel, Phys. Rev. B **41**, 11919 (1990).

[35] G. K. H. Madsen, J. Carrete, and M. J. Verstraete, BoltzTraP2, a program for interpolating band structures and calculating semi-classical transport coefficients, Comput. Phys. Commun. **231**, 140 (2018).

[36] J. Bardeen and W. Shockley, Deformation potentials and mobilities in non-polar crystals, Phys. Rev. **80**, 72 (1950).

[37] See Supplemental Material at http://link.aps.org/supplemental/10.1103/PhysRevB.104.075433 for (i) structural and magnetic ground states, (ii) band structures, (iii) details for second-order perturbation theory analysis, and (iv) transport properties.

[38] A. V. Kolobov, P. Fons, J. Tominaga, B. Hyot, and B. Andre, Instability and spontaneous reconstruction of few-monolayer thick GaN graphitic structures, Nano Lett. **16**, 4849 (2016).

[39] A. Mogulkoc, Y. Mogulkoc, M. Modarresi, and B. Alkan, Electronic structure and optical properties of novel monolayer gallium nitride and boron phosphide heterobilayers, Phys. Chem. Chem. Phys. **20**, 28124 (2018).

[40] Z. W. Wu, J. Yu, and S. J. Yuan, Strain-tunable magnetic and electronic properties of monolayer CrI_3, Phys. Chem. Chem. Phys. **21**, 7750 (2019).

[41] P. H. Jiang, L. Li, Z. L. Liao, Y. X. Zhao, and Z. C. Zhong, Spin direction-controlled electronic band structure in two-dimensional ferromagnetic CrI_3, Nano Lett. **18**, 3844 (2018).

[42] A. S. Dhoot, C. Israel, X. Moya, N. D. Mathur, and R. H. Friend, Large Electric Field Effect in Electrolyte-Gated Manganites, Phys. Rev. Lett. **102**, 136402 (2009).

[43] B. Huang, G. Clark, D. R. Klein, D. MacNeill, E. Navarro-Moratalla, K. L. Seyler, N. Wilson, M. A. McGuire, D. H. Cobden, D. Xiao, W. Yao, P. Jarillo-Herrero, and X. Xu, Electrical control of 2D magnetism in bilayer CrI_3, Nat. Nanotechnol. **13**, 544 (2018).

[44] J. T. Ye, S. Inoue, K. Kobayashi, Y. Kasahara, H. T. Yuan, H. Shimotani, and Y. Iwasa, Liquid-gated interface superconductivity on an atomically flat film, Nat. Mater. **9**, 125 (2010).

[45] C. Song, R. Q. Zhang, L. Y. Liao, Y. J. Zhou, X. F. Zhou, R. Y. Chen, Y. F. You, X. Z. Chen, and F. Pan, Spin-orbit torques: Materials, mechanisms, performances, and potential applications, Prog. Mater. Sci. **118**, 100761 (2021).

[46] B. Yang, X. Zhang, H. Yang, X. Han, and Y. Yan, Nonmetallic atoms induced magnetic anisotropy in monolayer chromium trihalides, J. Phys. Chem. C **123**, 691 (2018).

[47] D. S. Wang, R. Q. Wu, and A. J. Freeman, First-principles theory of surface magnetocrystalline anisotropy and the diatomic-pair model, Phys. Rev. B **47**, 14932 (1993).

[48] A. Mogulkoc, M. Modarresi, and A. N. Rudenko, Two-dimensional chromium pnictides CrX (X = P, As, Sb): Half-metallic ferromagnets with high Curie temperature, Phys. Rev. B **102**, 024441 (2020).

[49] M. Modarresi, A. Mogulkoc, Y. Mogulkoc, and A. N. Rudenko, Lateral Spin Valve Based on the Two-Dimensional CrN/P/CrN Heterostructure, Phys. Rev. Appl. **11**, 064015 (2019).

[50] S. Memarzadeh, M. R. Roknabadi, M. Modarresi, A. Mogulkoc, and A. N. Rudenko, Role of charge doping and strain in the stabilization of in-plane ferromagnetism in monolayer VSe_2 at room temperature, 2D Mater. **8**, 035022 (2021).

[51] S. B. Chen, C. X. Huang, H. S. Sun, J. F. Ding, P. R. Jena, and E. J. Kan, Boosting the Curie temperature of two-dimensional semiconducting CrI_3 monolayer through van der Waals heterostructures, J. Phys. Chem. C **123**, 17987 (2019).

[52] G. K. H. Madsen and D. J. Singh, BoltzTraP. A code for calculating band-structure dependent quantities, Comput. Phys. Commun. **175**, 67 (2006).

[53] K. Durczewski and M. Ausloos, Nontrivial behavior of the thermoelectric power: Electron-electron versus electron-phonon scattering, Phys. Rev. B **61**, 5303 (2000).

[54] K. Ren, Y. Luo, S. Wang, J. P. Chou, J. Yu, W. C. Tang, and M. L. Sun, A van der Waals heterostructure based on graphene-like gallium nitride and boron selenide: A high-efficiency photocatalyst for water splitting, ACS Omega **4**, 21689 (2019).

[55] W. J. Yin, X. L. Zeng, B. Wen, Q. X. Ge, Y. Xu, G. Teobaldi, and L. M. Liu, The unique carrier mobility of Janus MoSSe/GaN heterostructures, Front. Phys. **16**, 33501 (2021).

[56] W. B. Zhang, Q. Qu, P. Zhu, and C. H. Lam, Robust intrinsic ferromagnetism and half semiconductivity in stable two-dimensional single-layer chromium trihalides, J. Mater. Chem. C **3**, 12457 (2015).